

# Unusual dust emission from planetary nebulae in the Magellanic Clouds

## Journal Item

The Astrophysical Journal, 699:1541–1552, 2009 July 10 doi:10.1088/0004-637X/699/2/1541


# UNUSUAL DUST EMISSION FROM PLANETARY NEBULAE IN THE MAGELLANIC CLOUDS

J. Bernard-Salas[1], E. Peeters[2,3], G. C. Sloan[1], S. Gutenkunst[1], M. Matsuura[4,5], A. G. G. M. Tielens[6], A. A. Zijlstra[7], and J. R. Houck[1]

[1] Center for Radiophysics and Space Research, Cornell University, 222 Space Sciences Building, Ithaca, NY 14853-6801, USA
[2] Department of Physics and Astronomy, The University of Western Ontario, London, ON N6A 3K7, Canada
[3] SETI Institute, 515 N. Whisman Drive, Mountain View, CA 94043, USA
[4] National Astronomical Observatory of Japan, Osawa 2-21-1, Mikata, Tokyo 181-8588, Japan
[5] Department of Physics and Astronomy, University College London, Gower Street, London WC1E 6BT, UK
[6] NASA Ames Research Center, MS 245-3, Moffett Field, CA 94035, USA
[7] Jodrell Bank Centre for Astrophysics, The University of Manchester, Manchester M13 9PL, UK
*Received 2008 September 3; accepted 2009 May 8; published 2009 June 24*

## ABSTRACT

We present a *Spitzer Space Telescope* spectroscopic study of a sample of 25 planetary nebulae (PNe) in the Magellanic Clouds (MCs). The low-resolution modules are used to analyze the dust features present in the infrared spectra. This study complements a previous work by the same authors where the same sample was analyzed in terms of neon and sulfur abundances. Over half of the objects (14) show emission of polycyclic aromatic hydrocarbons, typical of carbon-rich dust environments. We compare the hydrocarbon emission in our objects to those of Galactic H II regions and PNe, and Large Magellanic Cloud/Small Magellanic Cloud H II regions. Amorphous silicates are seen in just two objects, enforcing the now well known fact that oxygen-rich dust is less common at low metallicities. Besides these common features, some PNe show very unusual dust. Nine objects show a strong silicon carbide feature at 11 $\mu$m and 12 of them show magnesium sulfide emission starting at 25 $\mu$m. The high percentage of spectra with silicon carbide in the MCs is not common. Two objects show a broadband which may be attributed to hydrogenated amorphous carbon and weak low-excitation atomic lines. It is likely that these nebulae are very young. The spectra of the remaining eight nebulae are dominated by the emission of fine-structure lines with a weak continuum due to thermal emission of dust, although in a few cases the signal-to-noise ratio in the spectra is low, and weak dust features may not have been detected.

*Key words:* dust, extinction – infrared: general – Magellanic Clouds – planetary nebulae: general

## 1. INTRODUCTION

Dust forms at the end of the life of stars, during the asymptotic giant branch (AGB) phase (Gehrz 1989). Stars of low- and intermediate-mass progenitors experience strong mass loss during the AGB. For carbon stars, the radiation pressure on dust grains drives an outflow of gas which is coupled to and triggers the formation of molecules in a circumstellar envelope (e.g., Habing 1996). The mechanism driving the mass loss in oxygen-rich stars is still debatable. Woitke (2006) argued that the outflow in oxygen-rich stars cannot be driven by pulsations given the low near-infrared opacity of silicate grains, but he assumed models with only small amounts of iron in the grains. Adding iron increases the opacity, and iron is a significant component of interplanetary dust particles and may be present in AGB shells (Nguyen & Nittler 2008). Whatever the details of the envelope ejecta, the remaining envelope contracts onto a degenerate C–O core, and as the effective temperature rises the ultraviolet photons start to dissociate the molecules previously ejected (Bernard-Salas & Tielens 2005). At some point, ionization of the ejected gas will occur giving birth to the planetary nebula (PN) phase. A significant mass of the envelope will not be photodissociated, where molecules and dust will survive. These neutral regions in the interstellar medium where the chemistry and heating are governed by far-ultraviolet photons are referred to as photodissociation regions (PDRs; Hollenbach & Tielens 1999).

The peak of dust emission in planetary nebulae (PNe) occurs in the mid-infrared (mid-IR; ∼20–40 $\mu$m). The infrared spectra of these objects usually show dust features of either carbonaceous or silicate material. If the nebula is carbon-rich (C/O > 1), then most of the oxygen is locked into CO. This is a very stable molecule and the excess of carbon can form polycyclic aromatic hydrocarbons (PAHs), common in the spectra of a great variety of astronomical environments. If the nebula is oxygen rich, then the excess of oxygen can form amorphous and/or crystalline oxides and silicates.

A number of Galactic PNe show spectral evidence for both carbonaceous and silicate dust. These include PNe with WC central stars such as BD+30 3639, CPD−56 8032, and He 2–113 (Cohen et al. 2002; Bernard-Salas & Tielens 2005) as well as PNe resulting from very massive progenitors (like NGC 6302). In addition, some peculiar post-AGB objects (e.g., the Red Rectangle) also show evidence for mixed chemistry. Often the components are spatially separated with the silicates in a long-lived disk (Waters et al. 1998) and the carbonaceous dust in the outflow (Lloyd Evans 1990; Cohen et al. 1999). Observation of this dual chemistry in PNe spectra is independent of their gas phase chemical abundances within the PNe. The ratio of nebulae with double chemistry is higher in the bulge as shown by Gutenkunst et al. (2008) where out of 11 objects, six display both PAH and silicates features, and it is probably linked to their binary evolution or to a late phase of carbon-rich mass loss. In particular, a long-lived stable disk may trap early (O-rich) ejecta through a subsequent C-rich mass-loss phase in such binary systems.

Our general understanding of how these dust features form and evolve is still poor. For instance, PAH bands are known to vary not only in strength but also in profile; however, the cause of these variations is still not known. Some hypotheses

have included effects of metallicity, radiation field, grain size, grain charge, and dust composition (Peeters et al. 2002; van Diedenhoven et al. 2004; Sloan et al. 2005; Boersma et al. 2008; Bauschlicher et al. 2008, 2009; Joblin et al. 2008; J. Cami, et al. 2009, in preparation). The PAHs in PNe show in fact a larger variation from object to object than in other astronomical environments (Peeters et al. 2002).

The *Infrared Space Observatory* (*ISO*) made possible the detailed study of the infrared spectra of many PNe in the Milky Way (MW). However, due to the lack of sensitivity, *ISO* could not observe spectroscopically PNe outside the Galaxy. The Large and Small Magellanic Clouds (LMC and SMC, respectively) offer a great opportunity to study the dust in PNe in a different (metal-poor) environment. The *Spitzer Space Telescope* with its enhanced sensitivity is more suited to study dust in the Magellanic Clouds (MCs). In a recent paper, Bernard-Salas et al. (2008) presented the high-resolution (HR) 10–37 $\mu$m spectra of a sample of 26 PNe in the MCs. In this paper, we present the results of the low-resolution modules on board the *Spitzer Space Telescope* which are more suited to the study of dust. These results are compared with those found in PNe in the Galaxy and to H II regions in an attempt to characterize the kind of dust present in the MC PNe and how it compares to the dust in the Galaxy.

Using *IRAS* data, Lenzuni et al. (1989) studied the properties of the dust of several hundreds of PNe. They found that the grain size and total dust mass decrease as the nebula evolves, which they attributed to sputtering and grain–grain collisions. Stasińska & Szczerba (1999) have argued, however, that this results from an artifact in their method of analysis. Recently, Stanghellini et al. (2007) used *Spitzer* spectra of a sample of 41 MC PNe to correlate the dust features with the physical parameters of the central stars and the PNe morphology. They find that the temperature of the dust decreases as the nebula evolves and that the production of dust decreases at lower metallicity when compared with Galactic PNe. In this paper, we focus on the characterization of the dust features, their dependence on the environment as given by the strength of radiation field, and how the features compare to H II regions and Galactic PNe.

The paper is organized as follows. The next section explains the observations and data reduction. In Section 3, we explore and analyze the hydrocarbon features. Two carbonaceous dust features which are prominent in our spectra, silicon carbide (SiC) and magnesium sulfide (MgS) are presented in Sections 4 and 5, respectively. A discussion on the silicate features is given in Section 6. Other features present in the Infrared Spectrograph (IRS) data are discussed in Section 7. Finally, the conclusions are presented in the last section.

## 2. OBSERVATIONS AND DATA REDUCTION

The observations were taken with the *Spitzer Space Telescope* (Werner et al. 2004) and were part of the IRS Guaranteed Time Observations (GTOs) program (ID 103). From this program, SMP LMC 11 is not included in this sample as its spectrum was already published in Bernard-Salas et al. (2006) and found to be a pre-PN. The observations consisted of high- and low-resolution spectra of 25 PNe taken with the IRS[8] (Houck et al. 2004). As mentioned in Section 1, we refer only to the results using the low-resolution modules (SL and LL). These modules cover a wavelength region from 5.5 to 37 $\mu$m with a resolution of 60–120. Details on the assumed coordinates and pointing strategy are given by Bernard-Salas et al. (2008). The data were taken using the IRS Staring Mode observing template which produces spectra in two *nod* positions (at 1/3 and 2/3 of the slit length). The spectral images were processed with the S13.2 version of the *Spitzer* Science Center (SSC)'s pipeline and using a script version of *Smart* (Higdon et al. 2004). The data reduction started from the *droop* files which are similar to the most commonly used *bcd* data and only lack the flat-field and stray-cross-light removal. The rogue pixels were removed using the *irsclean* tool which is available from the SSC Web site.[9] When different cycles were present for a given observation these were combined to improve the signal-to-noise ratio (S/N). This was done for each module and *nod* separately. Then, for a given module the two *nod* positions were differentiated to remove the contribution from the background (e.g., SL1 nod1 minus SL1 nod2 and vice versa). Spectra were extracted from the resultant two-dimensional images using variable column extraction, which is fixed to four pixels at the wavelength center of each module. The calibration was performed by dividing the resultant spectrum by that of the calibration star (which was

**Table 1**
Sources Classification

| Object | HE[a] | WR | PAHs[b] | SiC | MgS | Silicates | Other Feat.[c] |
|---|---|---|---|---|---|---|---|
| SMP LMC 02 | ... | ... | ... | ... | ... | ... | HAC |
| SMP LMC 08 | ... | ... | B, B | Y | Y | ... | Bump16 |
| SMP LMC 13 | Y | ... | B, B | ... | ... | ... | ... |
| SMP LMC 28 | Y | ... | ... | ... | ... | Y? | ... |
| SMP LMC 31 | ... | Y? | B, A | Y | Y | ... | Bump16 |
| SMP LMC 35 | Y | ... | ... | ... | ... | ... | ... |
| SMP LMC 36 | Y | ... | B, B | ... | Y | ... | Plateau15 |
| SMP LMC 38 | ... | Y | A, B | ... | Y | ... | Plateau15 |
| SMP LMC 40 | Y | ... | ... | ... | ... | ... | ... |
| SMP LMC 53 | ... | ... | ... | ... | ... | Y | ... |
| SMP LMC 58 | ... | Y | B, B | Y | Y | ... | Bump16 |
| SMP LMC 61 | ... | Y | B, B | ... | Y | ... | Plateau15 |
| SMP LMC 62 | Y | ... | ... | ... | ... | Y | ... |
| SMP LMC 76 | ... | ... | B, B | Y | Y | ... | Bump16 |
| SMP LMC 78 | Y | ... | AB, B | Y | Y | ... | Bump16 |
| SMP LMC 83[d] | Y | Y[e] | ... | ... | ... | ... | ... |
| SMP LMC 85 | ... | ... | B, B | Y | Y | ... | Bump16 |
| SMP LMC 87 | ... | ... | ... | ... | ... | ... | ... |
| SMP SMC 01 | ... | ... | AB, AB | Y | Y | ... | Bump16 |
| SMP SMC 03 | ... | ... | B, B | ... | ... | ... | ... |
| SMP SMC 06 | ... | Y | B, B | Y | Y | ... | Bump16 |
| SMP SMC 11 | ... | ... | A, A | ... | ... | ... | ... |
| SMP SMC 22 | Y | ... | ... | ... | ... | ... | ... |
| SMP SMC 24 | ... | ... | ? | Y | Y | ... | HAC |
| SMP SMC 28 | Y | ... | ... | ... | ... | ... | ... |

**Notes.**
[a] High-excitation PNe, those with [O IV] and [Ne V] lines.
[b] PAH classification of the 6.2 band and 7.7 $\mu$m complex, respectively, according to the scheme by Peeters et al. (2002).
[c] Other features. The Bump16 refers to the broad excess between 16 and 22 $\mu$m; Mol. Abs. indicates molecular absorption; Plateau15 refers to the underlying PAH plateau due to C–C–C modes at 15.5–20 $\mu$m; and HAC is the acronym for hydrogenated amorphous carbon.
[d] This object was presented in Bernard-Salas et al. (2004). It was part of the original program but was observed during In-Orbit Checkout.
[e] Instead of the usual [WC], SMP LMC 83 has a [WN] central star.

[8] The IRS was a collaborative venture between Cornell University and Ball Aerospace Corporation funded by NASA through the Jet Propulsion Laboratory and the Ames Research Center.

[9] http://ssc.spitzer.caltech.edu

extracted in the same way as the target), then multiplying by its template (Cohen et al. 2003; G. C. Sloan, et al. 2009, in preparation). The calibration stars used are HR 6348 for the SL module and HD 173511 for LL. Remaining glitches which were not present in both *nod* positions or in the overlapping region between orders were removed manually. We note that there is another source close to SMP-SMC11 in the SL slit, and may contaminate to some extent the PAH fluxes (between 10% and 40%) quoted in Table 1 for this source.

In some of the spectra a discontinuity is present between the different modules (∼10%–30% in flux). These discontinuities result from slight mispointings. We used coordinates given by Stanghellini et al. (2002, 2003) and Leisy et al. (1997) and performed peak-up acquisition which produces 0.″4 accuracy. However, the SL slit is very narrow (3.″6) and flux losses can occur if the coordinates are not very accurate. In fact, there are differences of 1″–2″ between the coordinates given by Stanghellini et al. (2002, 2003) and Leisy et al. (1997) when they have objects in common in their sample. The LL slit is 10.″5 across, wide enough to account for pointing uncertainties, and thus the rest of the spectra were scaled to match this module.

Figure 1 shows the extracted spectra, where the most prominent lines and features are marked in the top of the figure.[10] PAHs are present in most of the spectra, and two objects show amorphous silicates. No object is seen with mixed chemistry. Eight objects show no apparent PAHs or silicates and just a very weak continuum with strong forbidden lines. Table 1 gives a summary of the main features seen in the spectra and indicates the high-excitation PNe and those with Wolf–Rayet features.

## 3. HYDROCARBONS

### *3.1. PAHs*

Out of the PNe listed in Table 1, 14 of them show PAH features. In these objects, the most typical features at 6.2 $\mu$m, 7.7 $\mu$m, 8.6 $\mu$m, and 11.2 $\mu$m are always present. The 12.7 $\mu$m feature is detected in five of the PNe and the 16.4 $\mu$m band and 17 $\mu$m complex are seen in just three of the nebulae. The 11.2 $\mu$m band is in some cases on top of a broad SiC feature (see Section 4). This same SiC feature makes it difficult to detect the 12.7 $\mu$m complex in some of the objects. The small PAH bands at 6.0 and 11.0 $\mu$m are also seen.

#### *3.1.1. The Strength of the PAHs*

The strengths of the PAH emission features were determined by integrating the flux of the feature above an adopted continuum in the *nod*-combined spectra and are given in Table 2. The baseline for the continuum was derived by fitting a spline function to selected regions of the spectra around each PAH. The integration limits were set to the following values: 6.1–6.6 $\mu$m for the 6.2 $\mu$m PAH band, 7.20–8.3 $\mu$m for the 7.7 $\mu$m PAH, 8.3–8.88 $\mu$m for the 8.6 $\mu$m PAH, and 11.1–11.7 $\mu$m for the 11.2 feature. This method produced very solid results which were reproducible to within 5% for most objects. In some cases, the 11.2 $\mu$m PAH feature sits on top of a much broader and stronger SiC feature. To make sure that the continuum underlying this feature is well determined we overplotted the PAH profile of the Orion Nebula when measuring the feature. In addition, we measured this feature using the HR spectra presented in Bernard-Salas et al. (2008), where the features are better disentangled (but the spectra are more affected by rogue pixels), and found that the measured values in most of the cases were well within 10% (Table 2).

An important characteristic of the PAHs is that their emission is influenced by the degree of ionization in the PDR (Langhoff 1996; Allamandola et al. 1999). A mixture dominated by neutral PAHs will emit strongly in the 11.2 $\mu$m band, while the bands at 6.2 $\mu$m, 7.7 $\mu$m, and 8.6 $\mu$m are stronger in ionized PAHs. In Figure 2 the ratio of the 7.7 $\mu$m/11.2 $\mu$m PAH bands (ionized/neutral) is plotted against the 6.2 $\mu$m/11.2 $\mu$m (ionized/neutral) ratio for the MC PNe together with a representative sample of ratios in Galactic PNe, and compared with ratios found by Vermeij et al. (2002) for H II regions. Higher ratios indicate a higher degree of ionization because the 7.7 and 6.2 $\mu$m PAHs are stronger in ionized PAHs than the 11.2 $\mu$m PAH, and it can be seen that both ratios correlate well with each other. The correlation in the PNe has a slope of $1.3 \pm 0.1$, which agrees within uncertainties with the slope derived for the H II regions ($1.5 \pm 0.2$). Vermeij et al. (2002) hinted that the H II regions seem to follow a relation with metallicity; the MW H II regions having the largest ratios while LMC H II regions have somewhat lower values and the only SMC H II region in their sample has the lowest ratio. While this relation was hampered by the low number of objects (especially in the SMC) recently Lebouteiller et al. (2008) in their study of the three giant H II regions NGC3603 (in the MW), 30 Doradus (LMC), and NGC 346 (SMC) find that this metallicity relation holds for these regions as well. All other things being equal, when the metallicity decreases, the electron density in the PDR (due to C ionization) will decrease. This results in a decreased neutralization rate and hence a shift to a higher degree of ionization, which is contrary to the observations of the H II regions.

The PNe do not show such a segregation in metallicity, indeed the PNe in the MW, LMC and SMC are scattered all across Figure 2. This is not surprising considering that PNe are not a homogeneous sample; they all have different ages.

The five PNe with the highest PAH degree of ionization (Figure 2) are those with the highest SiC fluxes (SMP LMC 08, SMP LMC 31, SMP LMC 58, SMP LMC 85, and SMP SMC 01). This is not due to uncertainties in the determination of the PAH 11.2 $\mu$m flux above the SiC feature because the measured PAH flux in the HR spectra (where both the PAH and SiC can be clearly separated) yields the same flux as in the low-resolution measurements.

Gordon et al. (2008) studied the relation of the PAH features with the hardness of the radiation field. They find a trend of decreasing PAH equivalent width (EW) with hardness of radiation in M101. This correlation leads them to argue that the variations in the strength of the PAH features are mainly the effect of processing of the dust grains. While not shown, our sample does not show any clear trend of PAH EW with [Ne III]/[Ne II] ratio (or the sulfur ratio) with the points scattered along the plot. However, in Figure 1, the presence of PAHs in the spectra is anticorrelated with the presence of the [O IV] and [Ne V] lines (see Table 1). Surely, PAHs will not survive the hard radiation field needed to excite these ions, but because we are integrating over the whole nebula one could expect emission from PAHs in the PDR (in the neighborhood of H II regions). Some Galactic PNe with high-excitation lines also show PAHs (e.g., NGC 7027). Like in our sample, the larger sample studied by Stanghellini et al. (2007) also shows this trend, although a few objects with high-excitation lines show very weak PAHs. It is possible then, that if the radiation field is high enough in

[10] SMP LMC 83 is not shown in the figure because its spectrum was already presented in Bernard-Salas et al. (2004).

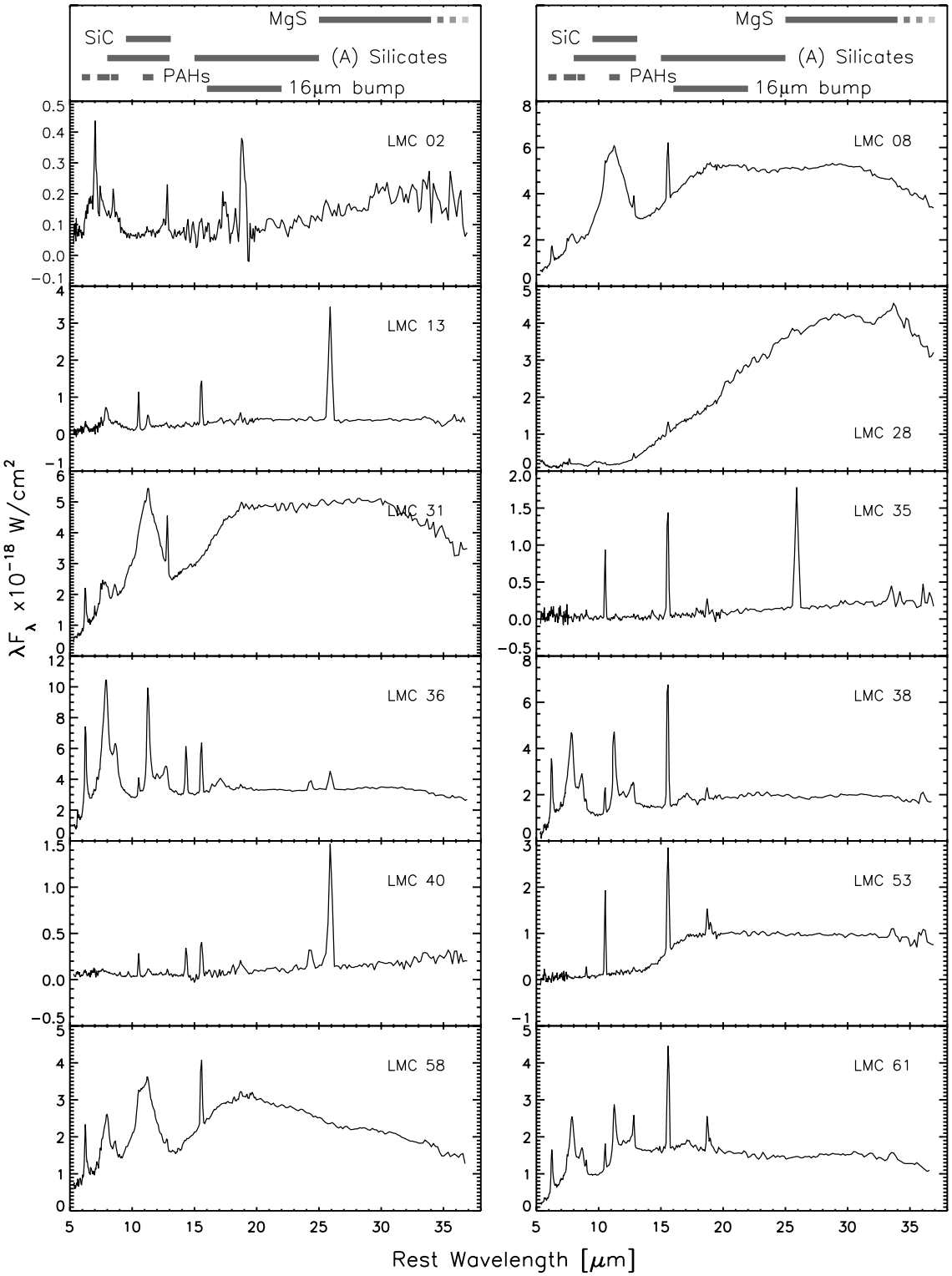


**Figure 1.** *Spitzer*-IRS's low-resolution spectra of the MC PNe. The most prominent bands are given in the legend (top panels).

the LMC and SMC, the PAHs are destroyed. The fact that this seems not to apply to the Galactic PNe may be ascribed to a size distribution.

### *3.1.2. Profiles*

It is well established that the profiles of the main PAH bands vary from object to object and spatially within extended objects (cf., Peeters et al. 2004, and references therein). Peeters et al. (2002) and van Diedenhoven et al. (2004) proposed a classification of the profiles of the main PAH bands based upon the *ISO* spectra of a variety of Galactic objects. In these studies, most PNe (all but five) belonged to class B, with the 6.2 $\mu$m PAH peaking between 6.24 and 6.28 $\mu$m, the 7.7 $\mu$m PAH between $\sim$7.8–8.0 $\mu$m and a redshifted 8.6 $\mu$m PAH band. The three exceptions are Hb 5, IRAS 21282+5050, and NGC 7027, which show a mixing in classes (e.g., class A for one feature and B

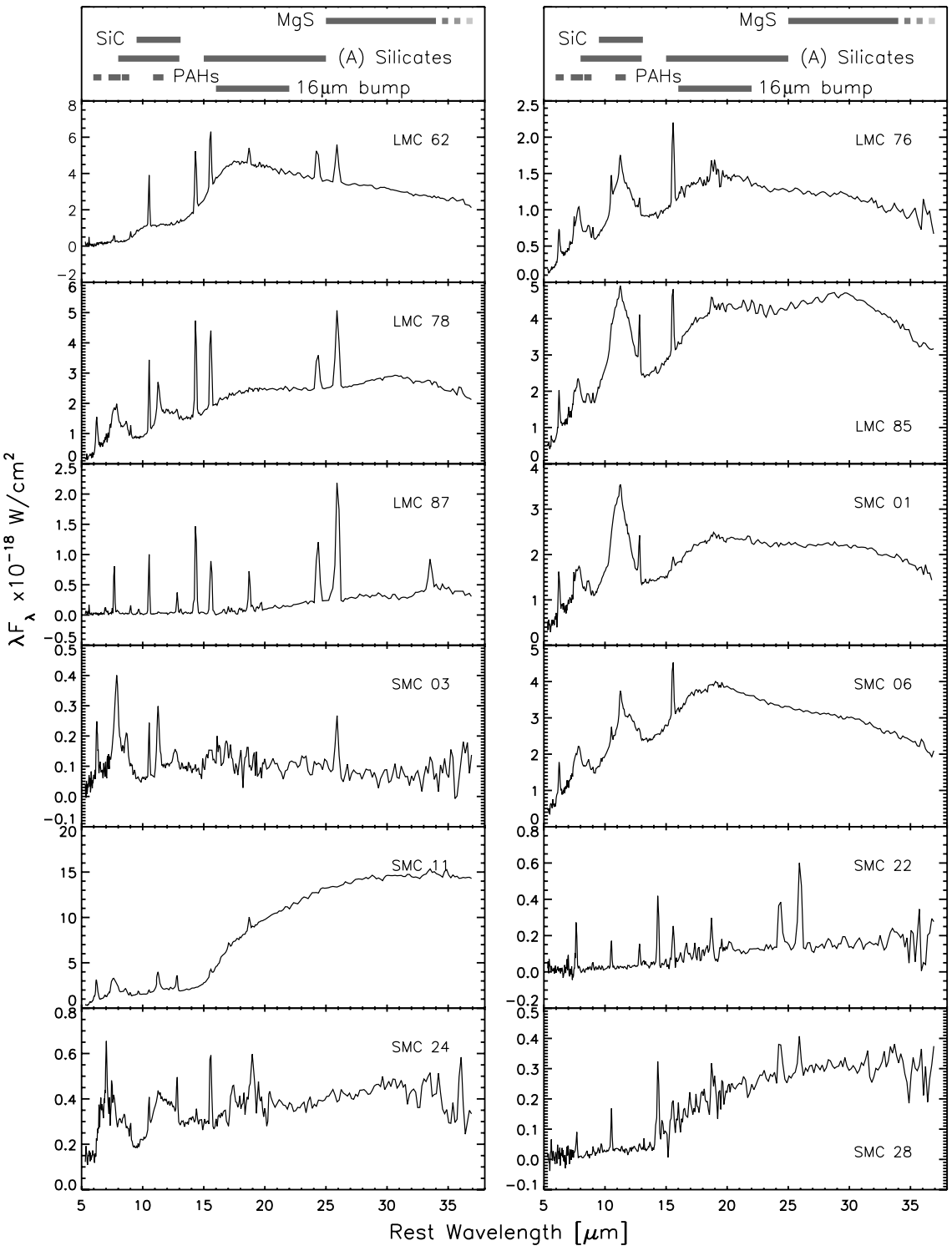


**Figure 1.** (Continued)

for others). The latter three sources together with BD + 30 3639 also have an 11.2 $\mu$m PAH profile belonging to class A(B).

Figure 3 shows the continuum-subtracted spectra of the PNe ordered according to the center wavelength of the 6.2 $\mu$m PAH (left panel), the 7.7 $\mu$m PAH (middle), and 11.2 $\mu$m PAH (right). The center wavelength is taken as the position at which the total flux of the feature is half and is used to derive the EW. The vertical lines and band indicate the nominal positions for the three classes in the Peeters et al. (2002) and van Diedenhoven et al. (2004) scheme. To guide the eye, the IRS spectra of Orion, which is a typical class A 6.2 $\mu$m band, is overplotted in black on top of each panel. Clearly, the low resolution of the SL and LL modules does not allow one to discern small variations (0.069 $\mu$m around 6–8 $\mu$m) as done in, e.g., Peeters et al. (2002), but it certainly can be used to study global trends, especially for the 7.7 $\mu$m complex. Hence, the IRS is still highly suitable to investigate PAH profile variations (e.g., Sloan et al. 2005, 2007). For instance, it can be seen from Figure 3 that the profile

**Table 2**
PAH and SiC Fluxes[a]

| Object | 6.2 $\mu$m | | 7.7 $\mu$m | | 8.6 $\mu$m | | 11.2 $\mu$m | | 11.2 $\mu$m (HR)[b] | | SiC | | SiC | |
|---|---|---|---|---|---|---|---|---|---|---|---|---|---|---|
| | Flux | Error | Flux | Error | Flux | Error | Flux | Error | Flux | Error | Flux | Error | EW[c] | Error |
| LMC-SMP08 | 2.22 | 0.08 | 3.71 | 0.13 | 0.63 | 0.04 | 0.81 | 0.08 | 1.18 | 0.03 | 55.98 | 0.35 | 23.21 | 0.32 |
| LMC-SMP13 | 0.67 | 0.09 | 1.99 | 0.28 | 0.09 | 0.09 | 0.85 | 0.04 | 0.91 | 0.01 | ... | ... | ... | ... |
| LMC-SMP31 | 3.54 | 0.18 | 5.30 | 0.27 | 1.28 | 0.06 | 1.05 | 0.05 | 1.25 | 0.06 | 46.90 | 0.09 | 22.31 | 0.04 |
| LMC-SMP36 | 16.01 | 0.56 | 25.63 | 0.36 | 3.70 | 0.14 | 14.50 | 0.16 | 14.03 | 0.12 | ... | ... | ... | ... |
| LMC-SMP38 | 6.94 | 0.13 | 12.55 | 0.31 | 2.67 | 0.22 | 6.86 | 0.11 | 5.45 | 0.04 | ... | ... | ... | ... |
| LMC-SMP58 | 4.50 | 0.10 | 5.71 | 0.26 | 0.82 | 0.12 | 1.03 | 0.08 | 1.07 | 0.03 | 29.72 | 0.31 | 21.40 | 0.28 |
| LMC-SMP61 | 3.65 | 0.05 | 6.07 | 0.17 | 1.00 | 0.05 | 3.23 | 0.10 | 3.23 | 0.05 | ... | ... | ... | ... |
| LMC-SMP76 | 1.47 | 0.03 | 2.05 | 0.12 | 0.41 | 0.05 | 0.81 | 0.03 | 0.87 | 0.02 | 11.43 | 0.21 | 17.19 | 0.35 |
| LMC-SMP78 | 3.49 | 0.12 | 6.00 | 0.45 | 0.85 | 0.23 | 2.65 | 0.26 | 2.93 | 0.02 | 8.52 | 1.27 | 8.75 | 1.48 |
| LMC-SMP85 | 2.71 | 0.11 | 3.93 | 0.43 | 0.71 | 0.10 | 0.78 | 0.06 | 0.86 | 0.06 | 45.12 | 0.43 | 24.65 | 0.40 |
| SMC-SMP01 | 2.15 | 0.13 | 3.51 | 0.37 | 0.75 | 0.07 | 0.93 | 0.05 | 0.97 | 0.03 | 30.39 | 0.28 | 26.84 | 0.51 |
| SMC-SMP03 | 0.52 | 0.03 | 1.27 | 0.04 | 0.23 | 0.02 | 0.49 | 0.01 | 0.51 | 0.02 | ... | ... | ... | ... |
| SMC-SMP06 | 2.95 | 0.14 | 3.61 | 0.21 | 0.38 | 0.18 | 2.34 | 0.18 | 2.12 | 0.04 | 18.42 | 0.84 | 10.61 | 0.55 |
| SMC-SMP11[d] | 6.43 | 0.12 | 8.78 | 0.35 | 1.39 | 0.10 | 4.47 | 0.16 | 4.92 | 0.11 | ... | ... | ... | ... |
| SMC-SMP24 | ... | ... | ... | ... | ... | ... | 0.15 | 0.03 | ... | ... | 3.47 | 0.17 | 19.88 | 1.28 |

**Notes.**
[a] Fluxes in units of $10^{-16}$ W m$^{-2}$.
[b] Measured in the HR spectra.
[c] EW is given in $\mu$m.
[d] PAH fluxes for this source may be contaminated by the presence of another source nearby (see Section 2).

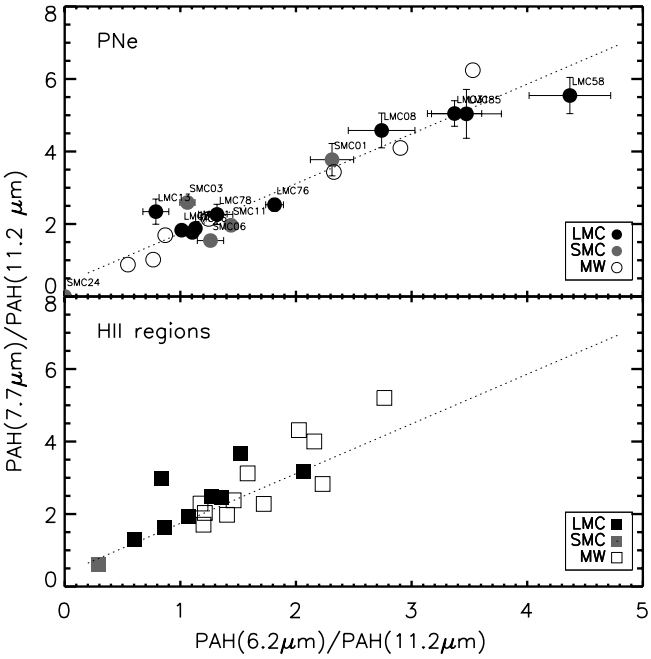


**Figure 2.** Ratio of ionized and neutral PAHs in PNe, compared with that of H II regions from the sample of Vermeij et al. (2002).

of the 6.2 $\mu$m PAH band shows variation in the onset of the blue wing and the peak position. Three PNe seem to be in the class A regime and the rest are in class B. Variations in the 7.7 $\mu$m complex are very obvious. The profile ranges from class A (lower two profiles) to class B. Note that while profiles of class A remain fairly similar, large variations are present within class B. The latter is actually defined as having a dominant "7.8" $\mu$m component of which the peak position and the entire profile can be redshifted considerably (Peeters et al. 2002). This can also be seen from Figure 3.

Small variations in the peak position of the 8.6 $\mu$m profile seem to be apparent as well. Unfortunately, due to the low spectral resolution no significant variations can be detected regarding the 11.2 $\mu$m PAH band profile (Figure 3). A possible exception could be SMP LMC 31. In general, sources exhibiting a class B 6.2 profile belong to class B for the other profiles as well. However, note that some PNe belong to mixed classed (e.g., SMP LMC 85).

There have been several hypotheses to explain the changes in wavelength of the peak of the PAHs. N-substituted PAHs (PANHs; Peeters et al. 2002; Hudgins et al. 2005) can produce emission at 6.2 $\mu$m. Indeed, pure PAHs exhibit emission longward of 6.3 $\mu$m in this specific region. Hence, within this framework, both pure PAHs and PANHs are needed to explain the observed variations. Recently, Bauschlicher et al. (2008, 2009) found that negatively charged PAHs are important in determining the overall emission spectrum, however, the spectra of negatively charged PANHs were not considered in the original studies of PANHs. Unlike for pure PAHs, the addition of an electron to PANHs redshifts the CC stretching mode, suggesting that charge variations in PANHs alone can explain the observed variations in the 6.2 PAH band (Bauschlicher et al. 2009).

The amount of blueshifting due to N-inclusion depends on the N/C ratio and the position of the N-atom inside the C skeleton (Hudgins et al. 2005). In a low-metallicity environment it may be expected that less nitrogen compared with carbon is available (due to the higher efficiency of the third dredge-up at low metallicities). Therefore, the relative fraction of pure PAHs with respect to PANHs may be higher in the MC, and as a consequence, the PAH emission bands may be more shifted to the red (assuming that a mixture of pure PAHs and PANHs is needed). However, this does not seem to be supported by the considered sample. While some sources have indeed a class A 6.2 $\mu$m profile, the observed variations in the MC PNe are also similar to those observed in our MW. Certainly, it would be interesting to look at the C/N abundance ratio to investigate this more thoroughly, but reliable determinations of C and N abundances are lacking in our sample.

The ratio of $^{13}C/^{12}C$ has also been proposed to explain the observed variations in the 6.2 $\mu$m PAH band (Wada et al.

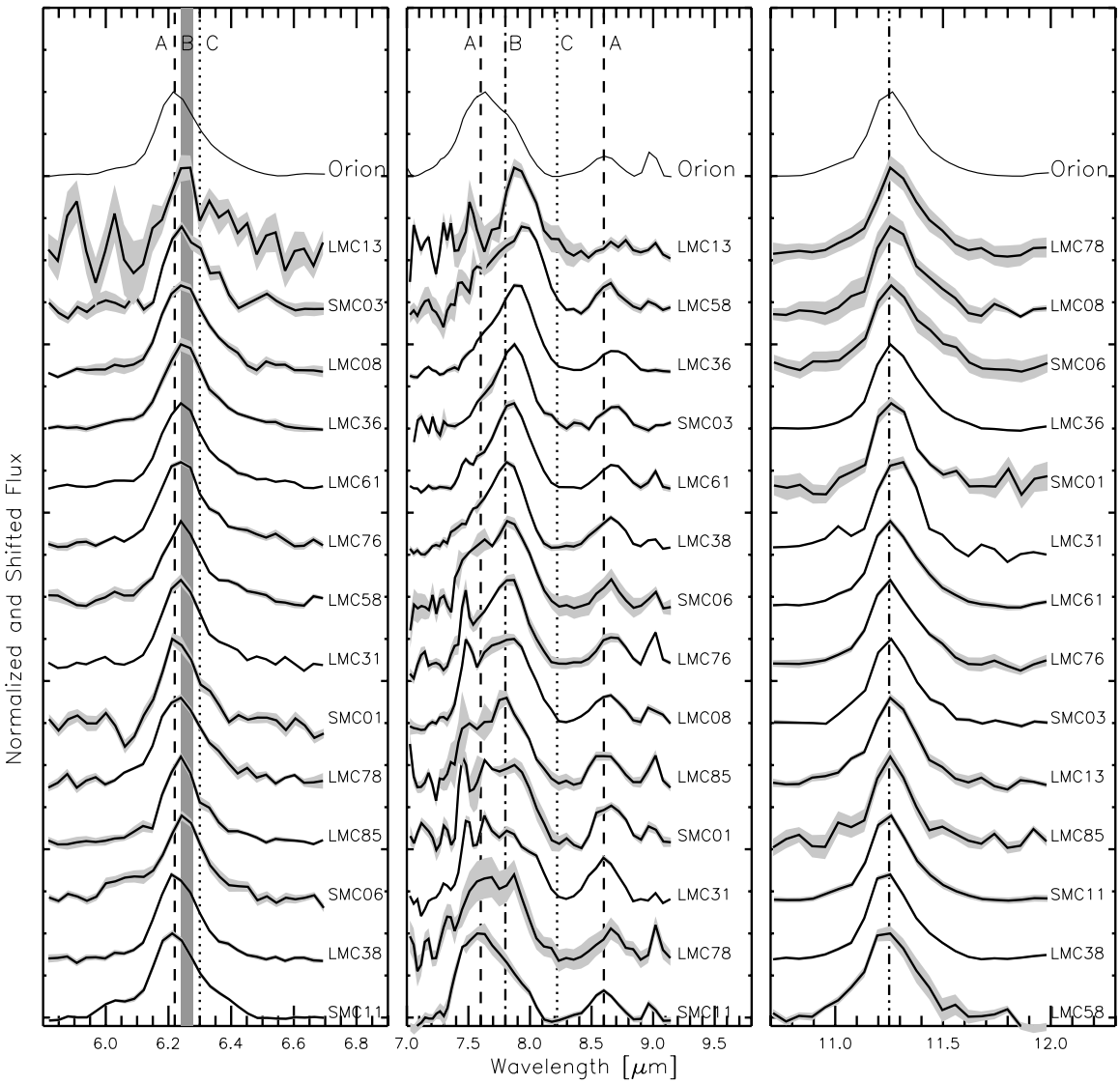


**Figure 3.** PAH profiles (in color) compared with that of Orion (thin black line). The profile classification given by Peeters et al. (2002) and van Diedenhoven et al. (2004) is given on the top of the figure. The gray area around a given spectrum indicates the uncertainty in the flux.

2003). However, while an enhanced $^{13}C/^{12}C$ ratio does shift the emission toward other wavelengths, it will redshift the emission. Given that pure PAHs exhibit emission longward of 6.3 $\mu$m in this region, enhanced $^{13}C/^{12}C$ in pure PAHs will not bring these bands toward 6.2 $\mu$m.

Laboratory and theoretical PAH spectra reveal that small and large PAHs emit at different wavelengths in the 7.7 $\mu$m region (Bauschlicher et al. 2008, 2009). In particular, small PAHs exhibit strong emission near ~7.6 $\mu$m, while large PAHs emit near ~7.8 $\mu$m. Bauschlicher et al. (2008, 2009) suggest that the observed difference between class A and class B sources is related to a variation in the size distribution of the PAH family. In addition, these studies revealed changes in the specific position of the emission near 7.7 $\mu$m with PAH charge. Large PAH anions emit at slightly longer wavelengths than PAH cations. Hence, variation in the peak position of the 7.8 $\mu$m component (and the 6.2 band, see above), and thus variation within the class B profiles, may be related to the variation in relative amount of large PAH cations and anions. Joblin et al. (2008) invoked a new component in their mathematical decomposition of observed PAH spectra with redshifted bands at 7.9 and 8.65 $\mu$m. These authors found that PAH anions may be plausible candidates for this component. Observationally, this charge dependence seems to be supported by the following studies. Peeters et al. (2002) found that the specific position of the 6.2 and 7.7 $\mu$m PAH bands are related to each other. Bregman & Temi (2005) found that the centroid of the 7.7 $\mu$m feature depends on $G_0/n_e$, which determines the charge balance in reflection nebulae.

Another mechanism can explain the shift in the PAH bands. There is increased observational evidence (Goto et al. 2000; Sloan et al. 2007) that the change in profile is in agreement with hydrocarbon mixtures that contain both aromatic and aliphatic bonds (see Section 3.3). In this scenario, in class C spectra the hydrocarbons are a relatively unprocessed mixture of aliphatics and aromatics, and as the radiation field becomes stronger the aliphatic bonds break to expose the aromatic bonds and give rise to class B and eventually class A spectra. This hypothesis has recently gained support from laboratory measurements of the 6.2 $\mu$m PAH feature by Pino et al. (2008) using carbonaceous soot. While they acknowledge that the astro-PAHs still need the right laboratory analogues, they have been able to reproduce the 6.3 $\mu$m peak using aliphatic material (class C) and the 6.2 $\mu$m

PAH (class A) with more mature PAHs. This line of work is very promising.

We have seen that the variations in peak position of the PAHs in the MCs are similar to those of their Galactic counterparts. The PAH profiles do not seem to vary significantly from Galactic PNe either. It seems that the overall conditions that produce the variations in the features in PNe are similar in the MW and in the MCs.

### 3.2. PAH Clusters

In addition to showing strong PAHs and having similar spectra, SMP LMC 36, SMP LMC 38, and SMP LMC 61 all have a plateau between 10 and 14 $\mu$m. These are the same three objects which do not show SiC but do show MgS (see Sections 4 and 5, respectively). This plateau has not been identified as any PAH overtone or combination of bands (Van Kerckhoven et al. 2000), but it has been suggested to be related to PAH clusters (Bregman 1989; Allamandola et al. 1989; Buss et al. 1993; Rapacioli et al. 2005; Joblin et al. 2008).

### 3.3. Hydrogenated Amorphous Carbon

The spectra of SMP LMC 02 and SMP SMC 24 show unusual emission of hydrocarbons between 6 and 9 $\mu$m, and the spectrum of SMP SMC 24 also shows smaller bumps at 17.5 $\mu$m and 19.5 $\mu$m (see Figure 1). The broad bump from 6 to 9 $\mu$m is similar (although it differs in detail) to that shown by the PPN IRAS 22272+5435. Buss et al. (1993) identified this emission with large hydrocarbons, e.g., PAH clusters and hydrogenated amorphous carbon (HAC). HAC has been observed at 3.4 $\mu$m in IRAS 22272+5435 by Goto et al. (2003), and it is therefore possible that the 6–9 $\mu$m emission in these nebulae is due to HAC.[11] Aliphatics are also seen in the IRS spectrum of the pre-PN SMP LMC 11 (Bernard-Salas et al. 2006), which shows many molecular absorption bands that are the building blocks from which more complex hydrocarbons are produced. In addition, Kraemer et al. (2006) detected $C_2H_2$ (with aliphatic bonds) as well as class C PAHs in the post-AGB star MSX SMC29. Goto et al. (2003) and Sloan et al. (2007) propose that carbonaceous materials are synthesized as large HAC compounds, and that the aliphatic bonds are broken as they get exposed to harder radiation fields, eventually leaving only aromatic bonds (those of PAHs). Joblin et al. (2008) find that the broad feature at 8.2 $\mu$m, which is associated with HAC, is more enhanced in young PNe. In this view, the possible presence of HAC in SMP SMC 24 and SMP LMC 02 would indicate that these PNe are very young. This is strengthened by the fact that only weak fine-structure lines of very low ionization potential are seen in the spectra of both objects.

## 4. SILICON CARBIDE

Figure 1 shows that most of the carbon-rich PNe have a broad feature from ~9 to 13 $\mu$m which peaks between 10.8 and 11.7 $\mu$m. We identify this feature as SiC. This feature is very prominent and explains the high *IRAS* flux ($F_{12}/F_{25}$) derived by Zijlstra et al. (1994) for some of these sources.

The SiC band is rare in Galactic PNe; from the available *ISO*-SWS PNe sample only IC 418 shows the feature, and it is also present in M1-20 from UKIRT spectra (Casassus et al. 2001). However, the SiC band is commonly seen in Galactic AGB stars. Stanghellini et al. (2007) propose an evolutionary sequence, where the SiC is seen in young PNe where PAHs are not yet formed. They make this claim based on the weak PAHs that are seen when the SiC is present in their sample. In our sample we see no such relation, with several sources showing strong PAH and strong SiC emission. Besides, if the suggestion by Stanghellini et al. (2007) was correct it should also hold for the MW, but hardly any MW PNe show SiC, while the PAHs are similar in the MW and MC. Thus, there should be another reason related to the environment that influences SiC formation and emission. As in the sample of Stanghellini et al. (2007), the PNe in our sample with SiC also have the smallest diameters,[12] hinting at an evolutionary process, but also maybe suggesting to a slower expansion velocity. At lower metallicities the mass loss may be slower because there is less dust to drive the outflow. On the other hand, since the carbon in the dust is produced within the star, one may not expect a decreased (carbon dust) mass-loss rate with metallicity. Matsuura et al. (2007) and Sloan et al. (2008) did not find a relation between metallicity and mass loss in the sample of AGB stars in the Fornax galaxy that they studied. The SiC is inherited from the AGB phase. Likely, at lower metallicity, the transition from O-rich to C-rich occurs earlier in the evolution on the AGB, and hence much of the Si is channeled to a carbonaceous condensation (SiC) rather than an oxide (e.g., silicates).

We measured the SiC feature by integrating the continuum-subtracted spectra from 9 to 13.2 $\mu$m, and removing the flux of the 11.2 $\mu$m PAH feature and the [Ne II] line when present (Table 2). Our data suggest that the feature is highly sensitive to the radiation field (at least at the metallicities we are probing). While SiC is present in PNe with strong [Ne III] lines (41.0 eV), the feature is absent when either the [O IV] (54.9 eV) or the [Ne V] (97.1 eV) lines are detected. Thus, it seems that photons with energies of about 55 eV destroy SiC grains. Figure 4 plots the EW[13] of the SiC feature against the ratio of the [Ne III] (15.56 $\mu$m) to [Ne II] (12.81 $\mu$m) line fluxes measured by Bernard-Salas et al. (2008) which traces the hardness of the radiation field. The sample is unfortunately small but there is a clear tendency of lower SiC EW with increasing radiation field hardness. IC 418 also falls on this relation. The same tendency is seen if the [S IV] (10.51 $\mu$m) to [S III] (18.71 $\mu$m) line ratio is used. This corroborates the relation of the SiC with ionization.

Figure 5 shows the profile of the SiC feature. The 11.2 $\mu$m PAH feature has been removed, and the positions of the fine-structure lines of [S IV] and [Ne II] are indicated by the vertical lines. It is clear that the profile varies from source to source. This is interesting because in Galactic and MC AGB stars the feature is very constant in shape. For comparison the red SiC profile of the Galactic PN IC 418[14] and the blue profile of a post-AGB object which encompass most of our sources (although we have some bluer ones) are also shown. Several factors could be responsible for shaping the feature: shape, size, extinction, and structure of the grains.

[11] We identify the emission in SMP SMC 24 from 9 to 14 $\mu$m with SiC, but the feature also resembles that of IRAS 22272+5435. If HAC is responsible for the emission in the 6–9 $\mu$m region, it is possible that they also contribute to the region where SiC is emitting. However, the SiC EW measurement falls well within in the relation shown in Figure 4, and its profile in Figure 5 resembles other SiC profiles.

[12] The Galactic PNe IC 418 and M1-20 also have small sizes.

[13] The EW is plotted instead of the integrated flux because it is independent of distance.

[14] For M1-20 only 8–13 $\mu$m spectrum is available and no [Ne III] line could be measured.

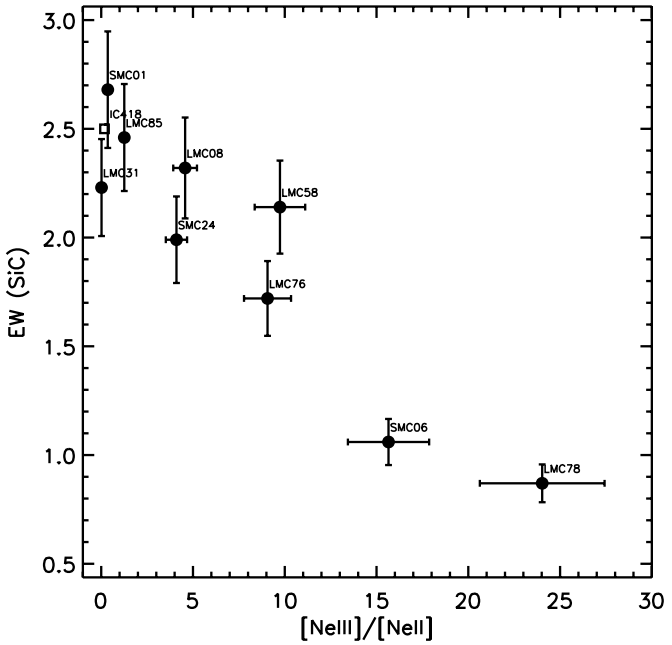


**Figure 4.** EW (in $\mu$m) of the SiC decreases with the hardness of the radiation field as given by the [Ne III]/[Ne II] ratio. The Galactic PN IC 418 is shown as an open square.

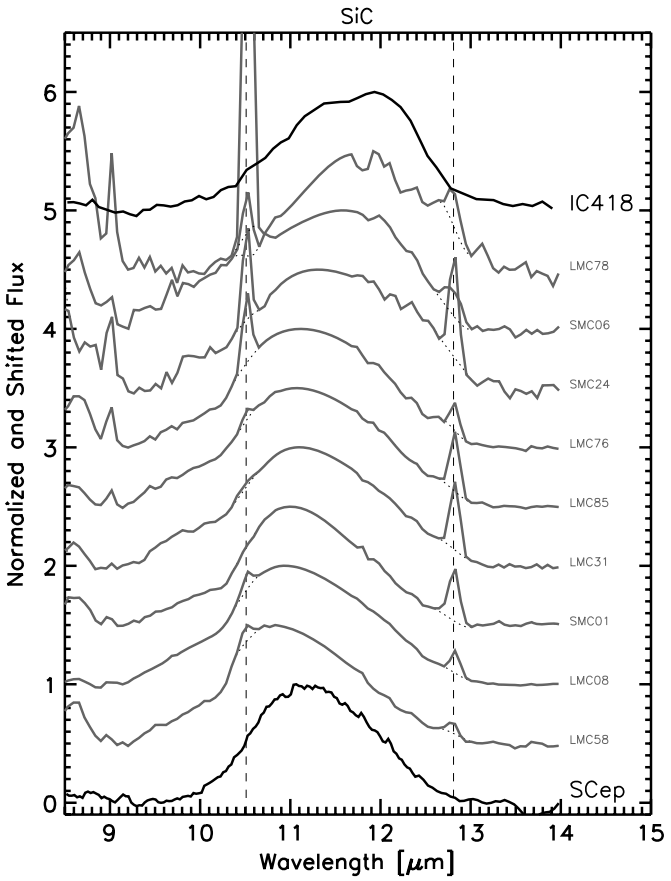


**Figure 5.** SiC feature in the MC PNe (in gray). The positions of the [S IV] and [Ne II] lines are indicated with the vertical lines with an underlying local continuum. For comparison, the SiC profile of the carbon star SCep and the PN IC 418 (in black) are also displayed.

Gilra (1972) and Treffers & Cohen (1974) first suggested that a distribution of shapes could produce the observed emission between longitudinal (10.3 $\mu$m) and transverse (12.6 $\mu$m) optical phonon modes. According to Speck et al. (2005), SiC at $\sim$10.85 $\mu$m can be reproduced with larger spherical grains, where the longitudinal mode becomes more significant. Clément et al. (2003) give an alternative explanation where the shift in position is attributed to different degrees of agglomeration of $\beta$-SiC nanoparticles (with agglomerated SiC shifting the feature to the red compared with nonagglomerated material). The change in position in our sample may reflect aggregation or changes in size, but it is also possible that a change in grain shape could produce the observed shift. We note that extinction is not likely to cause the variation of the SiC profile in our sample. SiC represents only a fraction of the dust, even in optically thick shells (e.g., Griffin 1990; Sloan & Egan 1995). Those rare cases where SiC is seen in absorption may be associated with a very short lived phase on the AGB (Speck et al. 2009). By the PN phase, the dust shell would have dissipated and once again be optically thin. The extinction in the sources is in fact very low with $E_{B-V}$ ranging from 0.04 to 0.36 (Bernard-Salas et al. 2008).

Comparisons between samples of Galactic AGB stars with other metal-poor carbon stars in the LMC (Zijlstra et al. 2006), SMC (Lagadec et al. 2007), and the Fornax dwarf spheroidal (Matsuura et al. 2007) show that the strength of the SiC feature decreases at lower metallicity. These studies argue that this is driven by the lower silicon abundance at lower metallicity. The observational evidence from the PNe seems to indicate that the silicon abundance is not the main driver of the feature (at least down to the SMC metallicity). The reason the feature is stronger in PNe than in AGB stars may be related to the higher temperature of the central star in the PN phase. In order to be sufficiently heated, SiC needs to be close to the central star (SiC absorbs shortward of 0.4 $\mu$m). Its presence in a disk may provide the necessary conditions for its formation. This incidentally could allow the grains to grow larger and could also affect its shape. Small grains cannot be ruled out. The strong SiC features in our spectra may be the result of a significant population of smaller grains instead of more SiC (by mass). This is consistent with the picture proposed by Speck et al. (2005) where the grains get smaller as the star evolves although it does not explain why it is not seen in Galactic PNe.

The condensation sequence of SiC is still a matter of debate. In their study of carbon stars, Lagadec et al. (2007) suggested that, based on the condensation temperatures of graphite and SiC, the SiC is deposited on carbon grains in the MC, while in the MW it is the other way around. Our observations agree with this sequence. Leisenring et al. (2008), in their IRS study of 19 AGB stars in the LMC, propose a more complex carbon condensation sequence which involves amorphous carbon, SiC, and MgS, based on the strength of these features and the mass-loss rate. For the MCs they favor a sequence SiC$\rightarrow$(C, SiC)$\rightarrow$MgS (with MgS coating a layer of C and SiC). In this view MgS needs a layer of SiC to be formed. In our sample, only SMP LMC 36, SMP LMC 38, and SMP LMC 61 show MgS but no SiC, and while the strength of the MgS feature has not been calculated it is clear that these three PNe present a very weak feature as compared with the rest of the sample (e.g., SMP LMC 08, SMP LMC 31). Furthermore, in this coating sequence proposed by Leisenring et al. (2008), MgS always ends up as the top outer layer. In this scenario MgS cannot be hidden, and thus the amount of sulfur depleted onto this feature cannot be used to explain the low sulfur abundance seen in some PNe (see the next section).

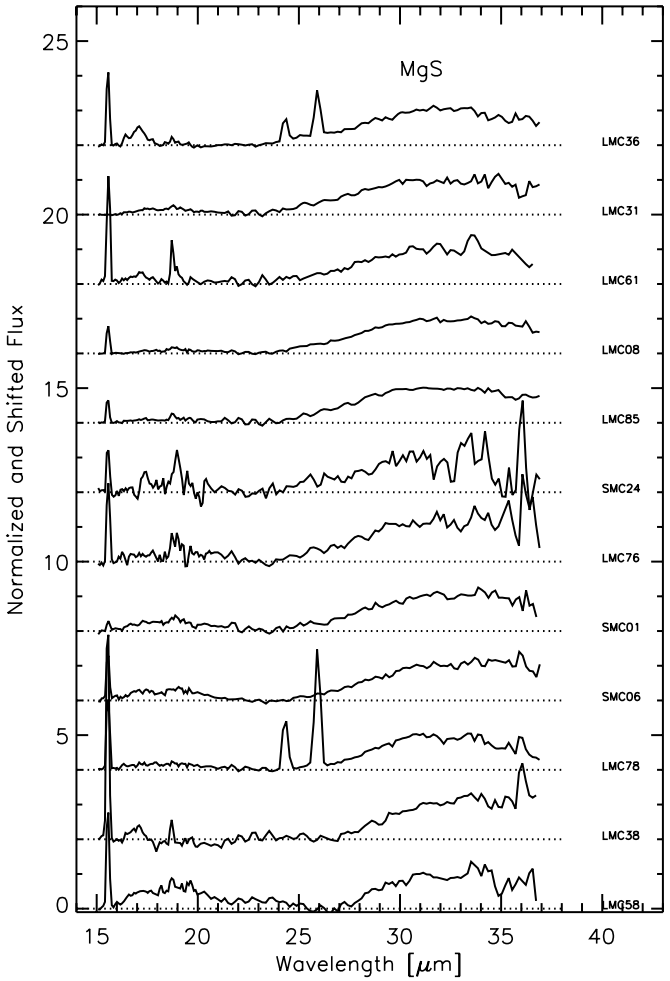


**Figure 6.** Continuum-subtracted spectra (see Section 5) of the 15–37 $\mu$m region to show the MgS feature. The feature at 16–21 $\mu$m is discussed in Section 7 and Figure 7.

## 5. THE 30 $\mu$m FEATURE

The "30 $\mu$m" feature has a long history, and it is common in the spectra of carbon stars and PNe. It usually extends from 25 to 45 $\mu$m, and was first discovered by Forrest et al. (1981). In the early stages it was tentatively identified as MgS by Goebel & Moseley (1985), but several other identifications were proposed shortly afterward (e.g., Duley 2000; Papoular 2000; Grishko et al. 2001). Hony et al. (2002) compiled a large number of *ISO* spectra of carbon stars and PNe and modeled the feature using MgS and a continuous distribution of ellipsoids with a grain temperature different from that of the bulk of the dust. In the same year, Volk et al. (2002) found that the feature could be resolved into two components, a narrow 26 $\mu$m and wider 33 $\mu$m feature in the SWS data, thus casting some doubts on MgS as the carrier of the feature. It has also been proposed that this structure at 26 $\mu$m is an artifact produced by the SWS overlapping region between bands 3D and 3E (Sloan et al. 2003) which is not very well calibrated. These two components can, however, be explained by differences in the shape distribution of MgS grains, where a stronger peak near 26 $\mu$m indicates more spherically shaped grains (S. Hony 2006, private communication). Within this frame one could speak of two MgS components; one more spherical and one less so. Despite the caveats, MgS is still the strongest candidate for this feature and we shall assume this for the discussion in the rest of the paper.

The feature is shown in Figure 6. Unfortunately, due to the wavelength coverage, the IRS modules miss the long-wavelength end of the feature, and the spectra also get noisy at long wavelengths. For this reason, we have not attempted to measure the strength of the feature because the measured flux would be unreliable. Much care was taken defining the underlying continuum, but the reader should bear in mind that while Figure 6 shows the PNe with MgS, the figure does not necessarily reflect the true strength of the feature. MgS is present in 12 of the PNe, all of the PNe showing PAHs except SMP LMC 36, SMP LMC 38, and SMP LMC 61, and in SMP SMC 24 where HAC may be present (Section 3.3). This feature can carry up to 30% of the infrared luminosity in the Galactic PNe and carbon stars (Hony et al. 2002). Therefore, if the feature is due to MgS a significant amount of magnesium and sulfur could be tied up in MgS. It is known that Galactic PNe show a sulfur depletion when compared with solar (Marigo et al. 2003; Pottasch & Bernard-Salas 2006). The sulfur abundances of six of the PNe in this sample are also lower than those found in MC H II regions (Bernard-Salas et al. 2008). This sulfur underabundance has even been seen in studies of H II regions in Local Group galaxies where it has also been suggested that maybe sulfur is depleted onto dust in these systems (Rubin et al. 2007). We tried to correlate the presence of this feature with the sulfur abundance but found no clear relation. Some PNe with MgS do show a low sulfur abundance but other PNe with MgS show normal sulfur abundances. This argues against sulfur being significantly depleted onto this feature (or against MgS being the carrier). There may be other sulfur-based features (e.g., FeS) on which sulfur is depleted, but none have been detected in the spectra.

## 6. SILICATES

The most common form of silicates are amorphous silicates, with features at 9.8 $\mu$m (Si–O stretching mode) and 18.5 $\mu$m (O–Si–O bending mode). Only two of the 25 objects in our sample show silicate emission, SMP LMC 53 and SMP LMC 62 (see Figure 1). SMP LMC 53 does not show the 9.8 $\mu$m stretching mode. This is normal and there are not many Galactic PNe with this feature either (e.g., NGC6302, NGC6543, Mz3). This is because as the nebula expands, silicate dust grains cool and are less efficient at emitting at 10 $\mu$m. There are no signs of the presence of crystalline silicates in our sample, even in the HR spectra. In the sample of Stanghellini et al. (2007) there are three additional oxygen-rich PNe (two in the LMC and one in the SMC). Adding them to our sample results in four oxygen PNe in the LMC out of 44, and one in the SMC out of 23. In the Galactic sample, the ratio of PNe showing oxygen-rich dust (silicates) compared with carbon-rich dust (PAHs) is higher than in the MCs. This has been found before in the study of AGB stars by Matsuura et al. (2007) where they found that the number of carbon-rich stars in the MCs was larger than expected. The reason for this is the decrease of the mass limit ($\sim$1.5 $M_{\odot}$ for the MW) at which the third dredge-up occurs at lower metallicities (Marigo et al. 2003). This dredge-up essentially mixes large amounts of $^{4}$He and $^{12}$C during thermal pulses and turns the envelope of the star carbon rich (C/O $>$ 1). In addition, the original lower oxygen content means that less carbon is needed to turn the C/O ratio larger than 1 Sloan et al. (2008). Therefore, we expect a larger number of PNe with carbon-rich chemistry than oxygen-rich ones at lower metallicity.

SMP LMC 28 shows a feature around 33 $\mu$m. This feature could be attributed to crystalline silicates but other expected

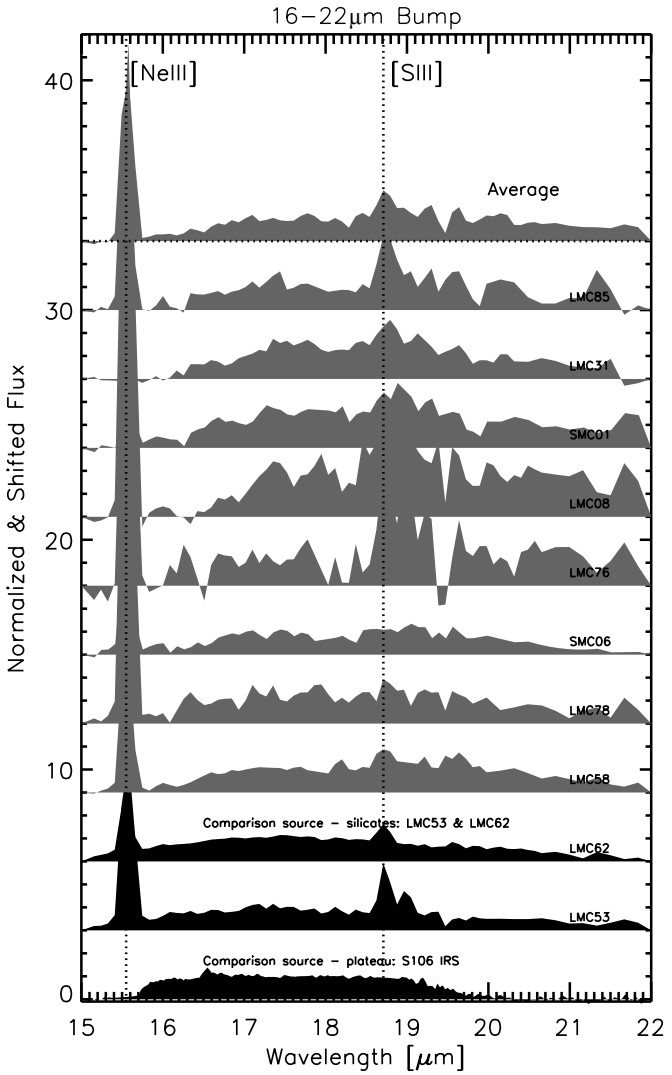


**Figure 7.** Continuum-subtracted spectra (see Section 6) of the 15–22 $\mu$m region. The "bump" in the sources (gray) is compared with two PNe with amorphous silicates and a YSO with a typical PAH plateau emission (black).

crystalline features at 28 and 23 $\mu$m are not detected. Lowering the temperature of the crystalline silicates (less than 100 K) weakens the 23 and especially the 28 $\mu$m features, but given the caveats, we leave this identification as tentative.

## 7. OTHER FEATURES

Many of the PNe display some kind of structure from around ~16 to 22 $\mu$m (Figure 7). This feature could simply be the result of dust peaking at 20 $\mu$m giving the spectrum a peculiar shape, but black- and gray-body fits (although uncertain to some degree) cannot match the region which should be dominated by emission of very small grains. If the peculiar shape is in fact a feature, the identification is not clear. Some features emitting around these wavelengths include: (1) the C–C–C PAH bending mode which produces a plateau from 15 to 20 $\mu$m; (2) amorphous silicates (O–Si–O stretching mode); and (3) the still unidentified 21 $\mu$m feature (Hrivnak et al. 2000; Hony et al. 2001). The feature is difficult to isolate because of the many other features present in the spectra (PAHs, plateaus, SiC, MgS) which make it difficult to determine a local continuum. However, we fitted a gray-body function (Hony et al. 2002) to the spectrum and compared with similarly fitted spectra of a YSO with a PAH plateau (S106 IRS) and two PNe with amorphous silicates from our own sample (SMP LMC53 and SMP LMC62). Figure 7 shows this comparison. The PAH plateau is clearly different from the feature and can be ruled out. The feature resembles amorphous silicates, and although the comparison is still not convincing, the reader should bear in mind the difficulty in assessing the continuum. If it were silicates it would then mean that a large fraction of the PNe presented here show a dual chemistry (PAHs and silicates). The 21 $\mu$m feature was first identified in PPNe by Hrivnak et al. (2000) and was later detected in some PNe by Hony et al. (2001). While not shown, we have compared the bump with *ISO*-SWS spectra of evolved objects showing the 21 $\mu$m feature, and the bump is distinctly very different in profile and position, ruling this identification out.

In SMP SMC 11 the continuum is very peculiar, showing a bell-like shape starting around 15 $\mu$m. Metal oxides could be a possible constituent to produce this excess emission (B. Sargent & W. Forrest 2008, private communication). Although the spectrum is noisier, the continuum in SMP SMC 28 is similar to that of SMP SMC 11 with the dust continuum steepening very suddenly after 12 $\mu$m. The peak of the dust continuum of these two sources lies between 30 and 35 $\mu$m, indicating cold dust with respect to the rest of the sample.

## 8. SUMMARY AND CONCLUSIONS

We have presented low-resolution spectra taken with the *Spitzer Space Telescope* of 25 PNe in the MCs (18 in the LMC and seven in the SMC). This is the same sample of objects examined at higher resolution by Bernard-Salas et al. (2008), but now we focus on the analysis of the dust features. The spectra show the typical features seen in Galactic PNe, but additionally some objects show very unusual dust.

Out of the 25 PNe, 14 show dust features characteristic of carbon-rich dust such as amorphous carbon and PAHs. Only two objects (SMP LMC 53 and SMP LMC 62) display oxygen-rich dust (amorphous silicates), and none show dual chemistry. The high proportion of nebulae with carbon-rich dust in the MCs compared with Galactic PNe is expected and reflects the efficiency of the third dredge-up at lower metallicities.

The ratio of ionized versus neutral PAHs in the MCs and MW correlate well, with a slope of 1.3. This slope agrees with what is found for H II regions. However, while H II regions are segregated in metallicity (higher ionization with higher metallicity), the PNe spread all over the range of ratios. The profiles of the PAHs are also similar to their Galactic counterparts.

The similarity seen in the PAH bands contrasts with the strong SiC feature which is seen in nine of the MC PNe. This feature is commonly seen in AGB stars, but it is very rare in Galactic PNe (only two in the Galactic sample). All of these objects show PAHs as well. Several studies in the literature comparing AGB stars in the Galaxy, LMC, SMC, and the metal-poor Fornax dwarf spheroidal, observed that the SiC feature decreases at lower metallicities, and this makes our finding even more remarkable. While at lower metallicities one expects less silicon to be available, it may be that the lower critical abundance of silicon to significantly suppress the SiC feature is not reached at the metallicities of the LMC and SMC. The EW of the feature decreases with the hardness of the radiation field, and it is not seen in high-excitation PNe, hinting at the destruction of the feature in hard radiation fields or preventing its formation.

The "30 $\mu$m" feature usually attributed to MgS is seen in 12 nebulae, but because of the wavelength range coverage of the

IRS we are unable to reliably measure its flux. In recent studies, it has been suggested that sulfur may be depleted onto dust to explain the anomalous gas phase abundance of this element in many PNe and H II regions. However, we do not find a clear correlation of PN with MgS having a lower abundance of sulfur in the sample.

There are three PNe that show MgS but no SiC. Instead of SiC the spectra of these PNe show strong PAHs with a plateau from 10 to 15 $\mu$m. HAC may be present in SMP LMC 02 and SMP SMC 24, which would imply that these are young PNe. This is supported by the weak- and low-excitation lines in the spectra of these objects.

The IRS on board the *Spitzer Space Telescope* has shown that the dust in MC PNe is both similar to and different from that of Galactic PNe. This is important for understanding the influence of metallicity on the different dust features that are present in the mid-IR wavelength range. Future observatories such as *Herschel* and *James Webb Space Telescope* (*JWST*) will be great aids in complementing the on-going work of *Spitzer*. *Herschel* will allow the extension of the mid-IR region probed by *Spitzer* to much longer wavelengths, and *JWST* will make it possible to extend the study of PNe to the furthest galaxies in the Local Group.

We thank A. Speck, B. Forrest, and B. Sargent for insightful comments and discussions. This work is based on observations made with the *Spitzer Space Telescope*, which is operated by the Jet Propulsion Laboratory, California Institute of Technology under NASA contract 1407. Support for this work was provided by NASA through Contract Number 1257184 issued by JPL/Caltech.

## REFERENCES

Allamandola, L. J., Hudgins, D. M., & Sandford, S. A. 1999, ApJ, 511, 115
Allamandola, L. J., Tielens, A. G. G. M., & Barker, J. R. 1989, ApJS, 71, 733
Bauschlicher, C. W. Jr., Peeters, E., & Allamandola, L. J. 2008, ApJ, 678, 316
Bauschlicher, C. W., Jr., Peeters, E., & Allamandola, L. J. 2009, ApJ, 697, 311
Bernard-Salas, J., Peeters, E., Sloan, G. C., Cami, J., Guiles, S., & Houck, J. R. 2006, ApJ, 652, L29
Bernard-Salas, J., Pottasch, S. R., & Gutenkunst, S. 2008, ApJ, 672, 274
Bernard-Salas, J., & Tielens, A. G. G. M. 2005, A&A, 431, 523
Bernard-Salas, J., et al. 2004, ApJS, 154, 278
Boersma, C., et al. 2008, A&A, 484, 241
Bregman, J. 1989, in IAU Symp. 135, Interstellar Dust, ed. L. J. Allamandola & A. G. G. M. Tielens (Dordrecht: Kluwer), 109
Bregman, J., & Temi, P. 2005, ApJ, 621, 831
Buss, R. H., Tielenes, A. G. G. M., & Cohen, M. 1993, ApJ, 415, 250
Casassus, S., Roche, P. F., Aitken, D. K., & Smith, C. H. 2001, MNRAS, 327, 744
Clément, D., Mutschke, H., Klein, R., & Henning, Th. 2003, ApJ, 594, 642
Cohen, M., Barlow, M. J., Liu, X.-W., & Jones, A. F. 2002, MNRAS, 332, 879
Cohen, M., Megeath, T. G., Hammersley, P. L., Martin-Luis, F., & Stauffer, J. 2003, AJ, 125, 2645
Cohen, M., et al. 1999, ApJ, 513, L135
Duley, W. W. 2000, ApJ, 528, 841
Forrest, W. J., Houck, J. R., & McCarthy, J. F. 1981, ApJ, 248, 195
Gehrz, R. 1989, in Proc. IAU Symp. 135, Interstellar Dust, ed. L. J. Allamandola & A. G. G. M. Tielens (Dordrecht: Kluwer), 445
Gilra, D. P. 1972, in The Scientific Results from the Orbiting Astronomical Observatory, ed. A. D. Code (NASA SP-310; Washington: NASA), 295
Goebel, J. H., & Moseley, S. H. 1985, ApJ, 290, L35
Gordon, K. D., et al. 2008, ApJ, 682, 336
Goto, M., et al. 2000, A&AS, 141, 149
Goto, M., et al. 2003, ApJ, 589, 419
Griffin, I. P. 1990, MNRAS, 247, 591
Grishko, V. I., Tereszchuk, K., Duley, W. W., & Bernath, P. 2001, ApJ, 558, L129
Gutenkunst, S., Bernard-Salas, J., Pottasch, S. R., Sloan, G. C., & Houck, J. R. 2008, ApJ, 680, 1206
Habing, H. J. 1996, A&AR, 7, 97
Higdon, S. J. U., et al. 2004, PASP, 116, 975
Hollenbach, D. J., & Tielens, A. G. G. M. 1999, Reviews of Modern Physics, 71, 173
Hony, S., Waters, L. B. F. M., & Tielens, A. G. G. M. 2001, A&A, 378, L41
Hony, S., Waters, L. B. F. M., & Tielens, A. G. G. M. 2002, A&A, 390, 533
Houck, J. R., et al. 2004, ApJS, 154, 18
Hrivnak, B. J., Volk, K., & Kwok, K. 2000, ApJ, 535, 275
Hudgins, D. M., Bauschlicher, C. W., Jr., & Allamandola, L. J. 2005, ApJ, 632, 316
Joblin, C., Szczerba, R., Berné, O., & Szyszka, C. 2008, A&A, 490, 189
Kraemer, K. E., et al. 2006, ApJ, 652, L25
Lagadec, E., et al. 2007, MNRAS, 376, 1270
Langhoff, S. R. 1996, J. Phys. Chem., 100, 2819
Lebouteiller, V., et al. 2008, ApJ, 680, 398
Leisenring, J. M., Markwick-Kemper, F., & Sloan, G. C. 2008, ApJ, 681, 1557
Leisy, P., Dennefeld, M., Alard, C., & Guibert, J. 1997, A&AS, 121, 407
Lenzuni, P., Natta, A., & Panagia, N. 1989, ApJ, 345, 306
Lloyd Evans, T. 1990, MNRAS, 243, 336
Marigo, P., Bernard-Salas, J., Pottasch, S. R., Tielens, A. G. G. M., & Wesselius, P. R. 2003, A&A, 409, 619
Matsuura, M., et al. 2007, MNRAS, 382, 1889
Nguyen, A., & Nittler, L. R. 2008, AAS Meeting 212, Vol. 40, 196
Papoular, R. 2000, A&A, 362, L9
Peeters, E., Allamandola, L. J., Hudgins, D. M., Hony, S., & Tielens, A. G. G. M. 2004, in ASP Conf. Ser. 309, Astrophysics of Dust, ed. A. N. Witt, G. C. Clayton, & B. T. Draine (San Francisco, CA: ASP), 141
Peeters, E., et al. 2002, A&A, 390, 1089
Pino, T., et al. 2008, A&A, 490, 665
Pottasch, S. R., & Bernard-Salas, J. 2006, A&A, 457, 189
Rapacioli, M., Joblin, C., & Boissel, P. 2005, A&A, 429, 193
Rubin, R. H., et al. 2007, MNRAS, 377, 1407
Sloan, G. C., & Egan, M. P. 1995, ApJ, 444, 452
Sloan, G. C., Kraemer, K. E., Price, S. D., & Shipman, R. F. 2003, ApJS, 147, 379
Sloan, G. C., et al. 2005, ApJ, 632, 956
Sloan, G. C., et al. 2007, ApJ, 664, 1144
Sloan, G. C., et al. 2008, ApJ, 686, 1056
Speck, A. K., Cornman, A. B., Wakeman, K., Wheeler, C. H., & Thompson, G. 2009, ApJ, 691, 1202
Speck, A. K., Thompson, G. D., & Hofmeister, A. M. 2005, ApJ, 634, 426
Stanghellini, L., et al. 2002, ApJ, 575, 178
Stanghellini, L., et al. 2003, ApJ, 596, 997
Stanghellini, L., et al. 2007, ApJ, 671, 1669
Stasińska, G., & Szczerba, R. 1999, A&A, 352, 297
Treffers, R., & Cohen, M. 1974, ApJ, 188, 545
van Diedenhoven, B., et al. 2004, ApJ, 611, 928
Van Kerckhoven, C., et al. 2000, A&A, 357, 1013
Vermeij, R., Peeters, E., Tielens, A. G. G. M., & van der Hulst, J. M. 2002, A&A, 382, 1042
Volk, K., Kwok, S., Hrivnak, B. J., & Szczerba, R. 2002, ApJ, 567, 412
Wada, S., Onaka, T., Yamamura, I., Murata, Y., & Tokunaga, A. T. 2003, A&A, 407, 551
Waters, L. F. B. M., et al. 1998, Nature, 391, 868
Werner, M., et al. 2004, ApJS, 154, 1
Woitke, P. 2006, A&A, 460, L9
Zijlstra, A. A., van Hoof, P. A. M., Chapman, J. M., & Loup, C. 1994, A&A, 290, 228
Zijlstra, A. A., et al. 2006, MNRAS, 370, 1961